Marine Structures 75 (2021) 102881

Contents lists available at ScienceDirect

Marine Structures

journal homepage: http://www.elsevier.com/locate/marstruc

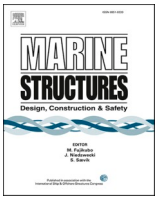

Crack growth direction effects on corrosion-fatigue behaviour of offshore wind turbine steel weldments

Anais Jacob, Ali Mehmanparast *

Offshore Renewable Energy Engineering Centre, Cranfield University, Bedfordshire, MK43 0AL, UK

ARTICLE INFO

Keywords:
Fatigue crack growth
HAZ
Simulated seawater
Offshore wind turbine monopile

ABSTRACT

In this study corrosion-fatigue tests have been conducted on fracture mechanics specimens extracted from an S355 G10+M structural steel welded plate. The tests have been performed on compact tension specimens with the crack tip located in the heat affected zone. The corrosion-fatigue test results from this study have been compared with the data available on the base metal as well as air tests on the same material. Moreover, the obtained results have been compared with the corrosion-fatigue data available in the literature on a wide range of steels and also the fatigue trends for welded joints in free-corrosion condition recommended in the BS7910 Standard. The effect of the specimen orientation, with respect to the weld region, is also examined in this study and it has been found that higher corrosion-fatigue crack growth rates are generally observed in the tests with 0° orientation. The results have also shown that the corrosive environment has significant effects on the fatigue crack growth acceleration at the beginning of the tests; however, as the crack propagates, the environmental damage effect on crack growth behaviour becomes less pronounced. The results presented in this study are discussed in terms of improvement in the structural integrity assessment of offshore wind turbine monopiles.

1. Introduction

Renewable energy is a reliable source of clean energy, which helps the international community to tackle greenhouse gas emission issues and contributes to meeting the increasing energy demand in the world. Among the different sources of renewable energy, offshore wind has become one of the most preferred solutions in recent years due to its large-scale deployment potential and significant reductions in its levelised cost, especially since 2016 [1–6]. The offshore wind turbine (OWT) installation, operation and in-service condition monitoring require consideration of a range of issues associated with the design and assessment of these structures. Indeed, due to the offshore turbulence and cyclic loads from wave, wind and current, these offshore structures are subjected to fatigue damage [7]. Moreover, for the OWT foundation, which is in direct contact with seawater, the additional environmental damage due to corrosion must also be considered and accounted for in design and life assessments. In order to withstand the critical conditions in harsh environments, the structural integrity of OWTs needs to be carefully assessed to provide a reliable estimate for the remaining life of these structures.

Among different types of existing OWT support structures, the monopile is the most popular foundation type which is widely used in shallow water offshore wind farms and has great design advantages as well as minimal footprint on the seabed [8,9]. Typical dimensions for the OWT monopile range from 50 m to 70 m in length, 3 m–10 m in diameter and 40 mm–150 mm in wall thickness

* Corresponding author.
E-mail address: a.mehmanparast@cranfield.ac.uk (A. Mehmanparast).

https://doi.org/10.1016/j.marstruc.2020.102881
Received 28 October 2019; Received in revised form 12 August 2020; Accepted 13 September 2020
Available online 24 October 2020

Nomenclature

a	Crack length
a_i	Initial crack length at the beginning of pre-fatigue cracking
a_0	Initial crack length at the beginning of the main fatigue test
a_f	Final crack length at the end of the main fatigue test
α	Normalised crack length
da/dN	Fatigue crack growth rate
A_p	Ramberg-Osgood non-linear stress coefficient
B	Specimen thickness
C	Paris-law coefficient
E	Elastic Young's modulus
f	Frequency
ΔK	Stress intensity factor range
K_{max}	Stress intensity factor corresponding to P_{max}
K_{min}	Stress intensity factor corresponding to P_{min}
m	Paris-law exponent
M	Ramberg-Osgood non-linear stress exponent
N	Number of cycles
P_{max}	Maximum applied load
P_{min}	Minimum applied load
ΔP	Load range
r_p	Plastic zone size
W	Specimen width
ε	Strain
σ	Applied stress
σ_y	Yield stress
BFS	Back face strain
BM	Base metal
C(T)	Compact tension
EDM	Electrical discharge machining
FCG	Fatigue Crack Growth
HAZ	Heat Affected Zone
LEFM	Linear elastic fracture mechanics
OWT	Offshore wind turbine
RS	Residual stress
SAW	Submerged Arc Welding
SIF	Stress Intensity Factor
WM	Weld metal

[10–12]. Monopiles are installed by driving them into the seabed; hence the structure should withstand the hammering loads during installation which vary from site to site depending on the soil conditions. During operation in harsh offshore environments, monopiles are subjected to wind, wave and sea current cyclic loads, therefore they have to be designed for a certain fatigue life with suitable safety margins against failure. Moreover, they have to be designed to withstand the horizontal and vertical loads acting on the entire assembly, including the transition piece, tower and wind turbine blades. The manufacturing procedure for offshore wind monopile structures consists of rolling and bending large structural steel plates and subsequently welding them together in longitudinal and circumferential directions [13]. The design, fabrication and inspection of OWT monopile foundations are costly. Therefore, an important challenge for the offshore wind industry is to improve the current best practice for the structural design and integrity assessment of monopiles that are operating in the harsh offshore environments with constant exertion of wind and wave loads inducing corrosion-fatigue damage, particularly at the weld regions and in the presence of welding residual stresses (RSs). Materials used in offshore structures are mainly chosen from medium to high strength structural steels, with the yield stress values typically ranging from 275 to 460 MPa, due to their suitable mechanical properties and low cost [14]. The studies in the literature have shown that fatigue crack initiation and growth primarily occur at the weld toe, for the as-welded conditions, and at circumferential welds [6]. Depending on the welding procedure, the crack may propagate from the Heat Affected Zone (HAZ) into the Base Metal (BM) in the through thickness direction [6]. More information about the fatigue damage and loading analysis of the monopile foundations can be found in Ref. [15,16].

An inter-laboratory test programme (referred to as the Structural Lifecycle Industry Collaboration Joint Industry Project-SLIC JIP) was previously run to characterise the fatigue crack growth (FCG) behaviour of the monopile welded structures in both air and seawater in order to better estimate the remaining life of monopiles in the presence of fatigue cracks [6,17]. The primary focus of the

SLIC project was on S355 G8+M steel; however, there is an essential need to extend the experimental investigations to other sub-grades of steel that are employed in the fabrication of monopiles and compare their FCG behaviour with those obtained from S355 G8+M steel in Ref. [6]. In the current study, the FCG behaviour of S355 G10+M structural steel, which is another sub-grade of steel that is widely used in the fabrication of monopiles, has been experimentally investigated in a seawater environment and the results have been compared with the material's behaviour in air as well as corrosion-fatigue crack growth behaviour in other steels. The results obtained from this study provide a better understanding of the FCG behaviour of a wide range of steels and facilitate structural design and integrity enhancement of OWT monopiles in free-corrosion conditions.

2. Material selection and sample preparation

2.1. Welding process

The material used in this study is EN-10225:09 S355 G10+M, which is widely used in the fabrication of offshore structures including OWT monopiles, as explained in the Standard from Det Norske Veritas [14]. In S355 G10+M notation, the letter S indicates that the material employed in this study is a structural steel with a minimum yield stress of 355 MPa while G10 indicates the steel grade within the material groups specified in the EN-10225 standard and +M indicates the thermo mechanical rolling process. The multi-pass submerged arc welding (SAW) technique was used to fabricate a double V-grooved welded plate with a thickness of 90 mm. The solid wire electrode was EN ISO 14171-A (EN 756): S3Si and the chosen flux was EN ISO 14174: SA FB 1 55 AC H. Welding was conducted parallel to the rolling direction using run off, thereafter cut, at each end of the plate, as shown in Fig. 1(a). The BM plates were hot-rolled prior to welding and individual weld passes at each V-groove were applied with a pre-heat of 60 °C. Welding was conducted using three electrode wires providing a heat input of up to 3.0 kJ/mm and an inter-pass temperature of not more than 250 °C. Double V-groove welding was performed unevenly by initially filling the first machined V-groove (see Fig. 1(b)) at the inner wall using 18 weld beads and then machining a deeper V-groove on the opposite side (i.e. at the outer wall) and filling it in using 25 weld beads. The welded plate was not subjected to post-weld heat treatment to replicate common practice in the fabrication of monopiles in industry.

2.2. Specimen preparation

In order to facilitate transportation of the large welded plate (with the overall dimensions of 90 mm thickness × 800 mm length × 1300 mm width) a smaller section with 90 mm × 200 mm × 600 mm dimensions was extracted and used for fabrication of fracture mechanics tests specimens. This weld section was subsequently sliced into smaller sections with 90 mm × 16 mm × 600 mm dimensions using an electrical discharge machining (EDM) technique to extract one fracture mechanics specimen with 16 mm thickness from each slice. In order to extract the compact tension C(T), specimens for FCG tests from the desired location with respect to the weld region, the outer plane of the welded section was ground, polished and etched using a 10% Nital solution (Nitric acid in Methanol). After revealing the material microstructure by etching the surface, C(T) specimens were extracted with the crack tip located in the HAZ region at the intersection region between the two V-grooves where the longest straight HAZ region in through thickness direction exists for fracture mechanics testing. An example of a polished and etched slice with the schematic C(T) drawing and crack tip location is

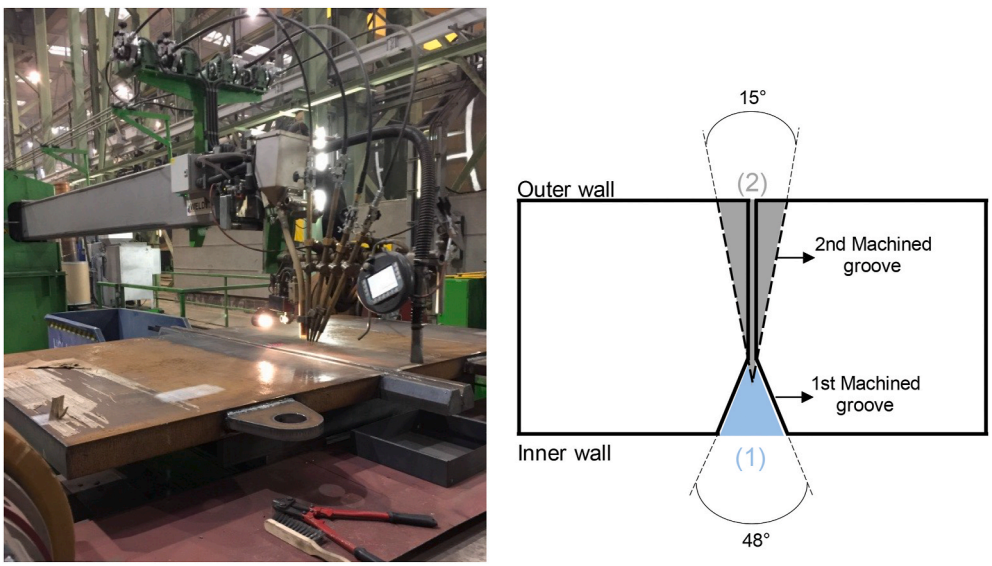

Fig. 1. Multi-pass submerged arc welding conducted on S355 G10+M BM plates; (a) welding process (Left), (b) schematic drawing of the machined V-grooves design and angles (Right).

shown in Fig. 2. As seen in this figure, the material microstructures were revealed after etching and the BM, HAZ, weld metal (WM) regions were identified before specimen extraction in order to locate the crack tip in the HAZ region. Also included in Fig. 2 are the transverse, longitudinal and normal directions with respect to the weld region.

As seen in Fig. 2, the C(T) specimens were extracted from each slice in such a way that the loading axis was parallel to the transverse direction, with respect to the weld region. This loading direction was chosen to replicate the loading conditions and direction in monopile weldments and performed through thickness crack propagation tests using the C(T) specimens. Also included in this study is the specimen orientation effect on the FCG behaviour of material in seawater. In order to do this, C(T) specimens were extracted with two orientations from the welded slices; the first set of specimens had the crack propagation direction, within the HAZ region, from the inner surface to the outer surface (see Fig. 2), which is referred to as the 0° specimen orientation, while the second set of specimens had the crack propagation direction from the outer surface towards the inner surface of the weld geometry, which is referred to as the 180° specimen orientation. The example shown in Fig. 2 demonstrates the extraction of a 0° specimen orientation (with the crack propagating from inner to outer surface) from a welded slice. Three C(T) specimens were extracted in each orientation with six nominally identical specimens prepared in total to perform FCG tests in this study. Two C(T) specimens (one specimen per orientation) were used to generate calibration curves by performing FCG tests in air, the details of which are explained in the next section, while the remaining four specimens were used to perform FCG tests in simulated seawater.

C(T) specimen extraction was conducted using EDM to eliminate the influence of machining and surface effects on subsequent FCG test results. C(T) specimens with a width of $W = 50$ mm, thickness of $B = 16$ mm and height of $H = 60$ mm were designed according to the ASTM E647 Standard test method for measurement of FCG rates [18]. Following the guidelines provided in ASTM E647 [18], a Chevron V-notch was included in the design of the C(T) specimens to introduce an initial crack length of $a_i = 17$ mm. All C(T) specimens were pre-fatigue cracked by approximately 4 mm to start the main FCG test with a crack length of around $a_0 = 21$ mm at the beginning of the test. The specimen pre-cracking from the initial V-notch tip was conducted using the K-decreasing approach, as recommended in Ref. [19], to control the level of crack tip plasticity during the pre-fatigue cracking process.

3. Fatigue crack growth test set-up

3.1. Calibration tests in air

The fatigue tests in this study were performed using a 100 kN servo-hydraulic Instron machine which was carefully calibrated and tuned prior to the start of each experiment. As mentioned earlier, two calibration tests (denoted C1 and C2 in Table 1) were performed in air to generate empirical correlations between the instantaneous crack length and the back face strain (BFS) measurement on the C(T) specimens. The details of the BFS technique are explained in Section 3.2 where the seawater set-up is explained and the BFS curves are used to estimate the crack lengths in seawater tests. As seen in Table 1, one calibration test was performed per specimen orientation. Also included in Table 1 are the specimen dimensions for C1 and C2 C(T) samples and the loading conditions. It can be observed in this table that the maximum and minimum applied loads in these two tests were $P_{max} = 10$ kN and $P_{min} = 1$ kN, respectively, the load ratio was $R = 0.1$ and the test frequency was $f = 5$ Hz. It must be noted that due to the dependency of the BFS calibration curves on the loading conditions, the applied load levels in calibration tests in air were exactly the same as those applied in seawater tests. The crack growth monitoring in calibration tests in air was conducted using two high resolution digital cameras located at the front and back of the test machine. Moreover, the variation in BFS values was continuously recorded throughout each test. Upon completion of the calibration tests, the average of the instantaneous crack length values obtained from the digital cameras was correlated with instantaneous BFS values to develop calibration curves for both 0° and 180° orientation specimens.

3.2. Seawater tests

Corrosion-fatigue tests were performed in the seawater environment on four C(T) specimens with the crack tip located in the HAZ, denoted S1, S2, S3 and S4 (see Table 1). The specimen dimensions and loading conditions for these tests are summarised in Table 1. As seen in this table, the applied loads on these four samples were $P_{max} = 10$ kN and $P_{min} = 1$ kN, with the load ratio of $R = 0.1$ and frequency of $f = 0.3$ Hz, which is the typical frequency used in corrosion-fatigue analysis of OWT monopile structures [6]. Also seen in Table 1 is that two corrosion-fatigue tests were performed on each of the specimen orientations (i.e. 0° and 180°). The tests were

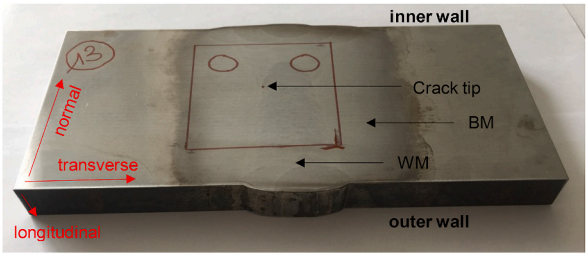

Fig. 2. An example of a welded slice for the extraction of C(T) specimens.

Table 1
C(T) specimen dimensions and loading conditions for corrosion-fatigue tests in seawater and calibration tests in air.

	C1	C2	S1	S2	S3	S4
Orientation (°)	180	0	0	0	180	180
a_i (mm)	17	17	17	17	17	17
a_0 (mm)	21.2	21.3	20.4	20.3	20.4	20.3
a_f (mm)	35.1	35.2	29.0	33.3	27.6	29.4
W (mm)	50	50	50	50	50	50
B (mm)	16	16	16	16	16	16
P_{max} (kN)	10	10	10	10	10	10
P_{min} (kN)	1	1	1	1	1	1
f (Hz)	5	5	0.3	0.3	0.3	0.3
r_p (mm)	0.17	0.17	0.17	0.17	0.18	0.17

conducted under load controlled mode and the load and position limits were set to ensure that the sample was not overloaded at any stage of the test, hence avoiding unexpected plasticity at the crack tip. Sinusoidal cyclic wave form using constant amplitude loading with a frequency of 0.3 Hz was used for corrosion-fatigue testing on the C(T) specimens.

In order to perform corrosion-fatigue tests on S1, S2, S3 and S4 C(T) specimens in free-corrosion conditions, 70 L of substitute seawater, using deionised water, was prepared in accordance with ASTM D1141-98 [20]. The composition of the artificial seawater prepared in the laboratory is given in Table 2. In these tests, due to the limited access to the test specimens soaked in seawater, which does not allow optical crack length measurement being employed in such experiments, the crack growth in the main corrosion-fatigue tests was monitored using the BFS technique. The basis of this approach is to correlate the bending strains at the back face of the C(T) specimens with the average crack length using the pre-existing calibration curves developed in air, for a given loading condition and specimen dimensions, and use these calibration curves to estimate the instantaneous crack length in seawater tests by continuously monitoring the change in the BFS measurements. In order to use the BFS technique for crack growth monitoring in seawater tests in this study, strain gauges were attached to the back face of the C(T) specimens and a polysulfide coating was applied to protect these gauges against seawater (see Fig. 3(a)). After attaching strain gauges to the C(T) specimens, the samples were soaked in seawater for approximately 48 h prior to testing, as recommended in the Standards [20] (see Fig. 3(b)). During corrosion-fatigue tests, the BFS measurements and number of cycles were recorded every 5 min throughout the test.

The experimental set-up for corrosion-fatigue tests is presented in Fig. 4. As seen in Fig. 4(a), a seawater environmental chamber was made of Pertex and located on the test machine to create a circulation of simulated seawater throughout the corrosion-fatigue tests. It can be observed in Fig. 4(b) that the created artificial seawater, which was stored in a reservoir, was running through the environmental chamber using pumps at a continuous rate of 4L/min. During the tests, the seawater temperature in the chamber was controlled using a Hailea refrigeration unit (see Fig. 4(b)) and varied between 7.5 °C and 8.2 °C to replicate the operational conditions in the North Sea. The pH level at the beginning of the experiment was 8.1, which decreased with time until a level of pH 7.7 was reached when the seawater was subsequently replaced. In total, 70 L of seawater were used for each experimental run where the specimen was completely immersed in the seawater throughout the test period.

3.3. Data analysis

The FCG rate, da/dN, in metals can be correlated with the linear elastic fracture mechanics (LEFM) parameter, ΔK using a power-law equation [21–24]:

$$da / dN = C(\Delta K)^m \tag{1}$$

In this equation, which is often referred to as Paris law, ΔK is the stress intensity factor range (SIF range), and C and m are material constants. According to ASTM Standard E647 [18], the equation which has been provided in this standard to calculate the SIF range for a C(T) specimen is valid for $a/W \geq 0.2$; however, it has been shown in Ref. [6] that the equation recommended in ASTM E647 encounters noticeable errors for $0.2 \leq a/W \leq 0.45$. An alternative equation that has been proposed in Ref. [6] for $0.2 \leq a/W \leq 0.7$ and

Table 2
Chemical composition of artificial seawater [20].

Chemical compound	Concentration (g/L)
$NaCl$	24.53
$MgCl_2$	5.20
Na_2So_4	4.09
$CaCl_2$	1.16
KCl	0.695
$NaHCO_3$	0.201
KBr	1.101
H_3BO_3	0.027
$SrCl_2$	0.025
NaF	0.003

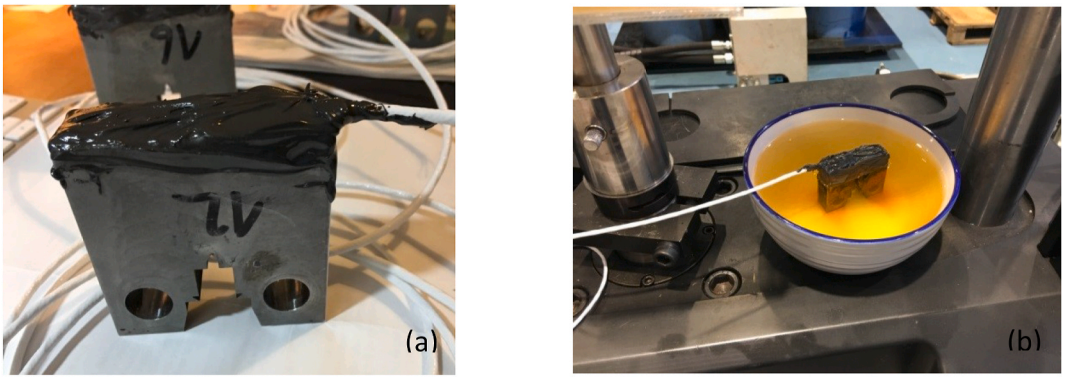

Fig. 3. (a) C(T) sample after strain gauging, (b) Specimen soaked in seawater prior to testing.

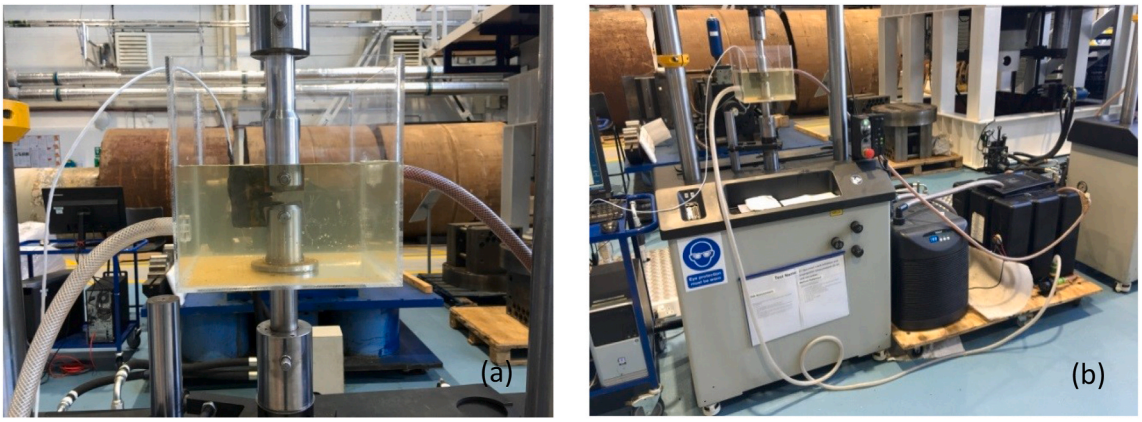

Fig. 4. (a) Pertex corrosion chamber, (b) Corrosion-fatigue crack growth test set-up.

has been used in this study is:

$$\Delta K = \left(\frac{\Delta P\sqrt{a}}{BW}\right)\left(-372.12\alpha^6 + 1628.60\alpha^5 - 2107.46\alpha^4 + 1304.65\alpha^3 - 391.20\alpha^2 + 54.81\alpha + 7.57\right) \quad (2)$$

where ΔP is the load range (i.e. ΔP=P_{max} - P_{min}), B is the specimen thickness, W is the specimen width and $\alpha = a/W$ is the normalised crack length.

The FCG rate, da/dN, in this study was calculated using the seven-point incremental polynomial method, except for the first and the last three data points for which the secant method was employed. To ensure that the level of plasticity introduced at the crack tip during the pre-fatigue cracking process is insignificant, and there is no plasticity effect on the FCG behaviour of the material in corrosion-fatigue tests, the plastic zone size at the beginning of the FCG tests (i.e. at the end of pre-fatigue cracking and beginning of the main FCG test where $a = a_0$) has been calculated using the following equation, and the results are included in Table 1 for each of the C(T) specimens tested in this study.

$$r_p = \frac{1}{\beta_1 \pi}\left(\frac{M-1}{M+1}\right)\left(\frac{K_{max}}{\sigma_y}\right)^2 \quad (3)$$

Equation (3) provides an estimate of plastic zone size in a cracked body for a power law hardening material subject to monotonic loading condition [25]. This equation is widely used to estimate the level of plasticity in cracked components and structures. In Equation (3), r_p is the plastic zone size ahead of the crack tip, M is the Ramberg-Osgood material model constant, K_{max} is the SIF at P_{max}, σ_y is the yield stress of the material and β_1 is a constant which is $\beta_1 = 3$ for plane strain conditions and $\beta_1 = 1$ for plane stress conditions. The plastic zone size calculations in this study have been performed under plane strain conditions by taking $\beta_1 = 3$.

In order to calculate the r_p values in the HAZ region ahead of the crack tip, the tensile curve for the S355 G10+M HAZ material, which was previously presented by authors in Ref. [13], was used to quantify the Ramberg-Osgood material model constants using the following equation [26,27]:

$$\varepsilon = \frac{\sigma}{E} + A_p \sigma^M \tag{4}$$

where ε is the total strain, σ is the applied stress, E is the elastic Young's modulus, A_p is the non-linear stress coefficient and M is the non-linear stress exponent. In Equation (4), the first term describes the elastic strain while the power-law term defines the non-linear plastic term in strain calculations.

The Ramberg-Osgood material model constants and elastic-plastic properties for S355 G10+M HAZ material are summarised in Table 3. The r_p values calculated using the HAZ material properties given in Table 3 and the loading conditions provided in Table 1 have been calculated for each test and the results are included in Table 1. The plastic zone size calculations show that in all six specimens the r_p values subsequent to pre-fatigue cracking are negligible compared to the initial crack size at the beginning of the main FCG test, a_0. This indicates that plasticity did not have any influence on the subsequent FCG behaviour of the material in all six C(T) specimens tested in this study.

4. Corrosion-fatigue test results and discussion

The results from the corrosion-fatigue tests performed in this study are presented in this section and compared with the recommended trends in the BS7910 Standard for welded joints in free-corrosion conditions. Moreover, the results obtained have been compared with the corrosion-fatigue data from other steels and also the FCG data on S355 G10+M in air. Corrosion-fatigue is a complex cumulative damaging phenomenon which occurs in structures subjected to cyclic loading in a corrosive environment, such as seawater. All the corrosion-fatigue tests in the present study are performed under free-corrosion conditions, with no cathodic protection, to account for the worst case scenario in the structural integrity assessment of monopiles.

4.1. Calibration test results in air

The micro-strain, $\mu\varepsilon$, results obtained from the strain gauge records on C1 and C2 C(T) specimens, which were tested in air, are correlated with the crack lengths measured using the digital cameras in Fig. 5. These two empirical calibration curves generated using C1 and C2 specimens, with 180° and 0° orientations, respectively, are used to convert the BFS measurements into millimetres of crack length in seawater tests. As seen in Fig. 5, the BFS *vs.* crack length trends from the tests performed in air have been found to fall upon or close to each other. It is worth noting that these calibration curves were developed using the same loading conditions ($P_{max} = 10$ kN, $R = 0.1$) and specimen dimensions with respect to the C(T) specimens that were used in the corrosion-fatigue tests.

4.2. Crack growth results from seawater tests

After recording the BFS data from seawater tests, the instantaneous crack lengths were estimated using the calibration curves shown in Fig. 5. The estimated crack lengths from each of the seawater tests are plotted against the number of cycles and the results are presented in Fig. 6. It can be observed in Fig. 6 that a lower number of cycles (approximately three to four times lower) was required to reach the same crack length on the 0° orientation samples compared to the 180° orientation. The difference between the crack growth trends in specimens with different orientations can be associated with the microstructural effects in the weld section. This observation is in agreement with the tests performed on S355 G10+M in air, where the crack propagated faster in 0° orientation specimens. Similarly, the gradient in the crack propagation trends for a given number of cycles was greater on the S1 and S2 samples, with 0° orientation, compared to S3 and S4, with 180° orientation.

4.3. Corrosion-fatigue crack growth rate results

The FCG rates for the four samples tested in seawater are correlated with ΔK and the results are shown on the log-log axis in Fig. 7. Also included in this figure are the mean curves (solid lines) and the upper bound trends (dashed lines) for the two specimen orientations, 0° and 180°, considered in this study. The statistical curves for 0° and 180° orientations are shown in black and grey lines, respectively. The C and m Paris-law constants (see Equation (1)) obtained from the mean curves and the upper bound trends, which are the mean curves plus two standard deviation (2SD), together with the R^2 values from each trend line are summarised in Table 4. It can be seen in Fig. 7 and Table 4 that for a given value of ΔK, the FCG rate in seawater tests is on average around 50% greater in the 0° specimens compared to the 180° samples. Also seen in Fig. 7 and Table 4 is that the level of scatter is greater in the 0° orientation samples compared to the 180° specimens, hence a larger SD is observed in the 0° orientation data set. Moreover, it can be seen in Fig. 7 that some discrepancies are evident in the FCG data obtained from the 0° specimens and, although the line of best fit is showing a higher trend compared to the 180° specimens, the lower bound data on the 0° specimens fall upon or close to the 180° specimens, especially in the high ΔK region.

Table 3
Ramberg-Osgood material model constants for S355 G10+M HAZ material.

M	A_p	σ_y (MPa)	E (GPa)
8	5.92×10^{-24}	469	190

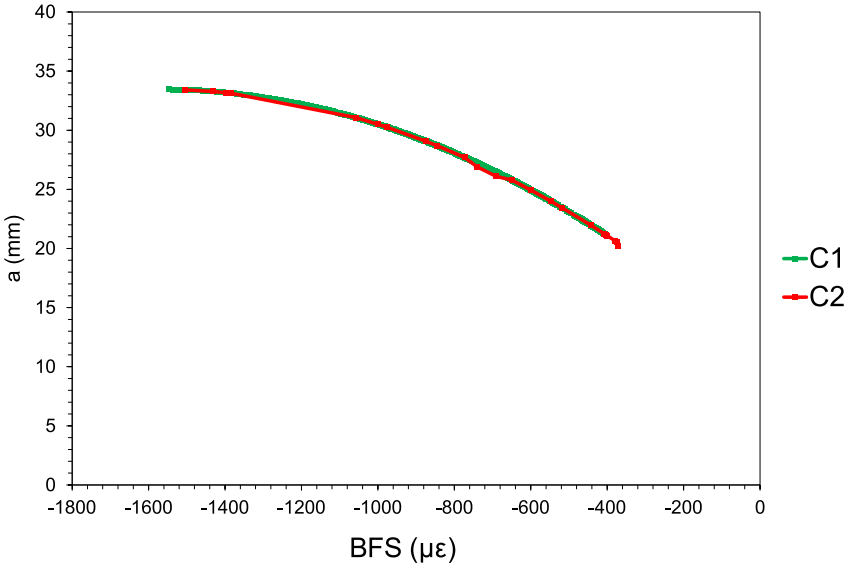

Fig. 5. Crack length *vs.* BFS results from calibration tests in air.

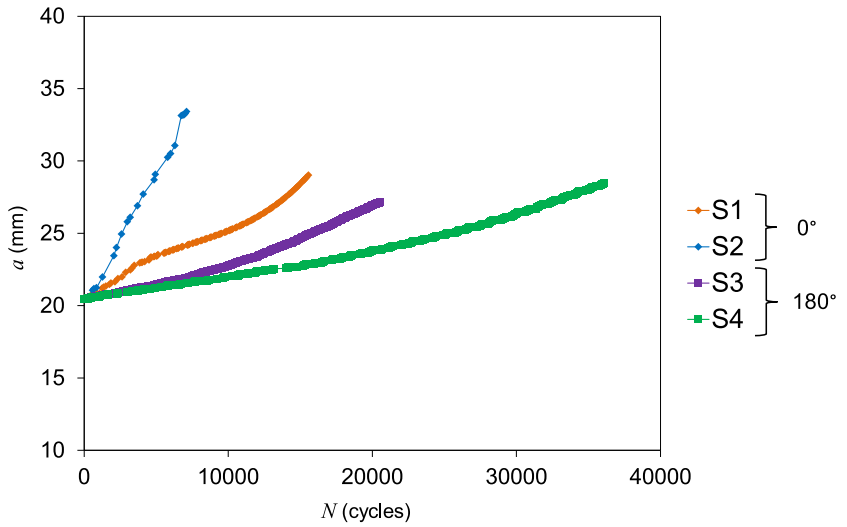

Fig. 6. *a vs. N* results from seawater tests.

These observations from seawater tests are consistent with those of made regarding specimen orientation effects in air tests in Ref. [1]. Considering the orientation of the specimens with respect to the weld region shown in Fig. 2, the seawater test results suggest that the corrosion-fatigue crack growth rate is lower when the crack propagates from the outside surface towards the inner surface of the monopiles. In other words, in order to estimate the lifetime of monopiles in the presence of macro cracks, more conservative predictions can be made by accounting for the Paris-law constants obtained from the 0° orientation samples. The results indicate that the FCG starting from the first welded V-groove machined on the inner surface of the monopile (i.e. 0° orientation samples) generally shows a higher trend, presumably due to the higher tensile residual stress levels which are introduced by welding the first V-groove. Having said that, residual stress measurements need to be conducted on the extracted samples in future work to confirm this hypothesis. The observations from this study are based on two tests on each specimen orientation; however, further tests and a comprehensive metallurgical analysis must be conducted in future work to confirm these preliminary results and capture a more realistic level of scatter for each orientation. It is worth noting that the weld mock-up used in the present study is a welded plate with flat inner and outer surfaces; however, the monopile fabrication processes, which include cold rolling and bending, must be considered in future work in order to examine the specimen orientation effects on FCG results in seawater in the presence of material pre-strains. It must also be noted that the results presented in this study are based on the global loading conditions; however, the remaining residual stresses in HAZ C(T) specimens need to be measured in future work to examine the significance of welding residual stresses in C(T)

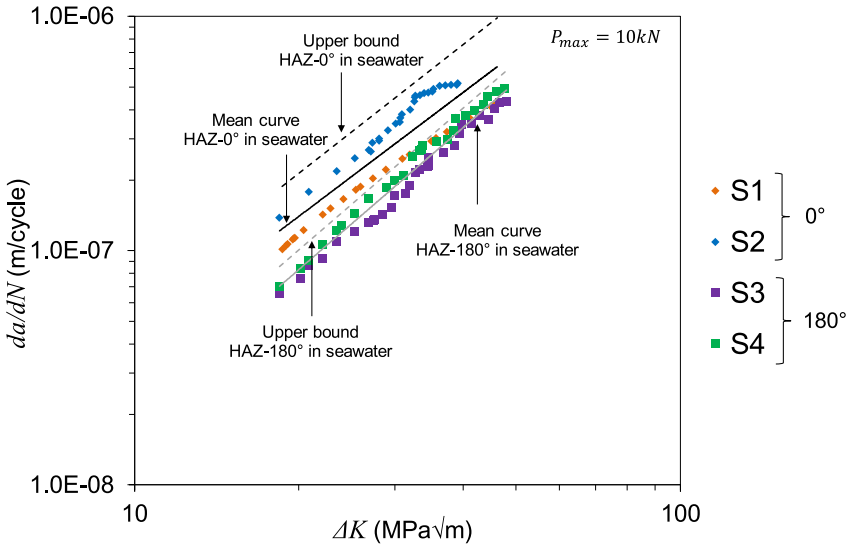

Fig. 7. Corrosion-fatigue crack growth rates and the lines of best fit for the tests in seawater.

Table 4
Paris law constants for seawater tests on two different specimen orientations.

	Mean curve			Mean + 2SD	
	C	m	R^2	C	m
0° orientation	5.6×10^{-10}	1.83	0.80	8.9×10^{-10}	1.83
180° orientation	2.0×10^{-10}	2.01	0.96	2.4×10^{-10}	2.01

specimens on the FCG behaviour of the HAZ material.

The FCG data from the seawater tests on both specimen orientations are compared with the FCG test results in air on the same material (denoted A1, A2 and A3 with 180° orientation and A4, A5 and A6 with 0° orientation), taken from Ref. [1], in Fig. 8. As seen in this figure, in both test environments the FCG trend for 0° orientations falls above the 180° orientation; however, this shift is greater in the air tests, especially in the lower ΔK region (i.e. around 100% higher) compared to the seawater tests (i.e. 50% higher). Also seen in this figure is that for the air tests, the observed slope in the FCG data is steeper than the seawater tests, though the seawater data generally lie above the air test data. Finally, it can be seen in Fig. 8 that the higher FCG rates in seawater tests, compared to air tests, are more pronounced in the lower ΔK region, though this difference reduces in the high ΔK region where the results from the tests in both environments begin to converge. The convergence of the FCG trends in air and seawater tests at the high ΔK region can be associated with the fact that due to the rapid crack propagation at larger crack lengths, there is not sufficient time for corrosion to contribute to the crack propagation process, hence the results from corrosion-fatigue tests start to become similar to those of the air tests. In other words, comparison of the FCG test data in air and seawater in Fig. 8 suggests that in corrosion-fatigue tests the corrosion damage is more pronounced in the low ΔK region, where the crack propagation rate is slower, but as the ΔK value increases corrosion damage becomes less dominant and eventually fatigue damage prevails.

The corrosion-fatigue crack growth data on S355 G10+M structural steel from S1, S2, S3 and S4 C(T) specimens in this study are compared with the corrosion-fatigue test data available on the BM (taken from Ref. [28]) and the results are shown in Fig. 9. Also included in this figure are the seawater HAZ data available from the SLIC project on S355 G8+M steel as well as similar steels from other studies and the proposed trends in BS7910 Standard [29]. It can be seen in this figure that the corrosion-fatigue data from the HAZ specimens with 180° orientation in the high ΔK region fall on top of the S355 G10+M BM corrosion-fatigue results obtained from the tests under the same loading conditions (P_{max} = 10 kN). It has also been noted that the SLIC corrosion-fatigue data, on S355 G8+M HAZ specimens, fall in between the upper and lower bound trends obtained from 0° to 180° specimen orientations examined in this study on S355 G10+M HAZ specimens. In general, the SLIC project data points fall closer to the 180° specimens from the present study.

The corrosion-fatigue HAZ data on similar steels taken from the literature are S355 G8+M [6], S355 J2+N [30], C-MN-V steel [31], 50D steel [32], API X70 steel [33], and RQ Tuf501 steel [34] which have been collectively compared with the new corrosion-fatigue data points from this study in Fig. 9. It can be observed in Fig. 9 that the corrosion-fatigue HAZ data from other steels generally fall upon or above the upper bound trend obtained from the current study on HAZ specimens with 0° orientation. Also seen in this figure is that for the dominant majority of the data points obtained from HAZ materials across a wide range of steels, the simplified law recommended in BS7910 provides a good fit to the upper bound data cloud. Moreover, it is seen in Fig. 9 that all data points from corrosion-fatigue tests on various BM and HAZ materials fall below the 2-stage law recommended for welded joints in free-corrosion in BS7910. Finally seen in Fig. 9 is that the line of best fit made to both 0° and 180° orientation specimens falls below the simplified and

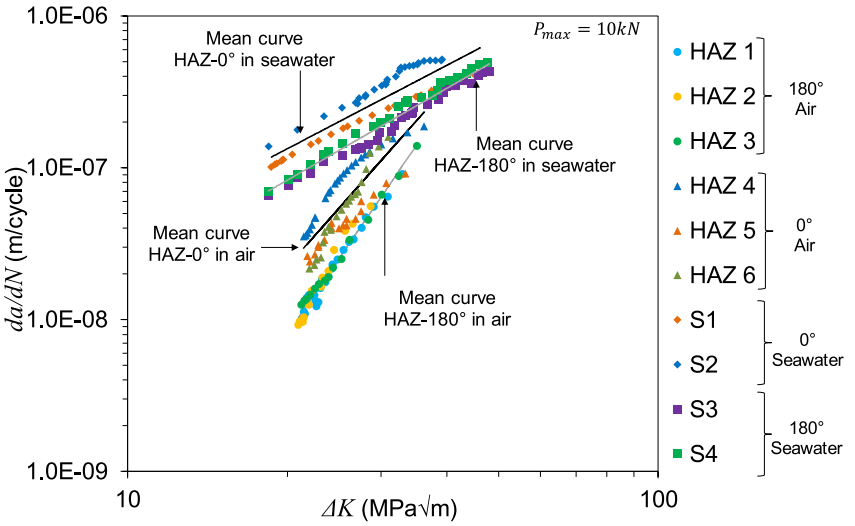

Fig. 8. Comparison of FCG rates in air and seawater.

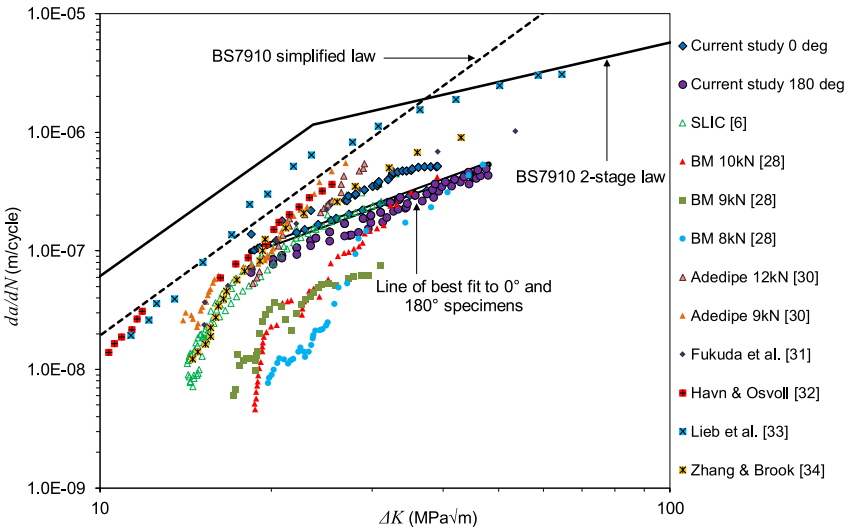

Fig. 9. Comparison of the FCG data in seawater with the literature data and BS7910 recommended trends.

2-stage FCG trends recommended by BS7910 with an average slope ($m = 1.8$) which falls in between the individual slopes observed in BS7910 2-stage law.

4.4. Post-mortem analysis

Upon completion of the corrosion-fatigue tests, the C(T) specimens were soaked in liquid nitrogen for 5 min and were subsequently broken open. Fractography analysis was performed on the fracture surface of all four corrosion-fatigue samples by taking high resolution pictures from the fracture surface and measuring the average through thickness final crack length in each sample using the ImageJ open source software [35]. It has been shown in previous studies that accurate crack length measurements can be achieved by performing image processing using this software [36–39]. An example of the broken open corrosion-fatigue test specimen is presented in Fig. 10 where the scale for converting pixels to mm can also be observed. The crack extension at the end of the test on all four samples has been measured on the fracture surface and the results are compared with the estimated crack extension values obtained using the BFS technique in Table 5. The crack extension, Δa, values in Table 5 are calculated as the difference between the final, a_f, and initial, a_i, crack length (before pre-fatigue cracking). As seen in this table, the maximum percentage error between the estimated and measured crack extensions at the end of the test in all four specimens is around 9%, indicating that acceptable estimations of the instantaneous crack lengths can be made by using the BFS crack growth monitoring technique for corrosion-fatigue tests. Further metallurgical analysis on the crack path and microstructural differences in various specimen orientations will be performed in future

Fig. 10. Fractography analysis on S1 specimen after break-open (the distance between division lines on the scale bar is 1 mm).

Table 5
Comparison of the measured and estimated crack extension values in corrosion-fatigue specimens.

	Crack extension estimated using BFS- Δa (mm)	Crack extension measured using optical imaging- Δa (mm)	% error
S1	16.3	15.2	7.2
S2	18.0	16.8	7.1
S3	16.0	14.9	7.4
S4	17.5	16.0	9.4

work to build a better understanding of the material microstructure effects on the FCG behaviour of the HAZ material in seawater.

5. Conclusions

Corrosion-fatigue tests have been performed on C(T) HAZ specimens extracted from an S355 G10+M welded plate. The experimental results have shown that, similarly to the air tests, the specimens with 0° orientation, with respect to the weld region, exhibit higher FCG rates in seawater tests compared to 180° orientation samples. This suggests that conservative analysis of the remaining life in OWT monopiles in the presence of macro cracks can be conducted by accounting for the Paris-law constants obtained from 0° orientation samples in seawater tests. Comparison of the FCG test data in air and seawater on S355 G10+M HAZ specimens shows that although a corrosive environment generally accelerates the FCG behaviour of the material, this effect is more pronounced at lower ΔK values and gradually diminishes as the crack propagates and the ΔK value subsequently increases. Also shown in this study is that the corrosion-fatigue data from the HAZ specimens with 180° orientation in the high ΔK region fall upon the BM data points obtained from the tests under the same loading conditions. Moreover, the corrosion-fatigue data on S355 G8+M HAZ specimens have been found to fall between the upper and lower bound trends obtained from this study on S355 G10+M. Finally, it has been observed that for the dominant majority of the data points obtained from HAZ specimens across a wide range of steels, the simplified law recommended in BS7910 provides a good fit to the upper bound data cloud.

Declaration of competing interest

The authors declare that they have no known competing financial interests or personal relationships that could have appeared to influence the work reported in this paper.

Acknowledgements

This work was supported by grant EP/L016303/1 for Cranfield, Oxford and Strathclyde Universities, Centre for Doctoral Training in Renewable Energy Marine Structures - REMS (http://www.rems-cdt.ac.uk/) from the UK Engineering and Physical Sciences Research Council (EPSRC). Anais Jacob would like to acknowledge ISIS-STFC financial support for her facility development studentship.

References

[1] Jacob A, Mehmanparast A, D'Urzo R, Kelleher J. Experimental and numerical investigation of residual stress effects on fatigue crack growth behaviour of S355 steel weldments. Int J Fatig Nov. 2019;128:105196.
[2] Owusu PA, Asumadu-Sarkodie S. A review of renewable energy sources, sustainability issues and climate change mitigation. Cicil Environ. Eng. 2016;3.

[3] Jensen PH, Chaviaropolos T, Natarajan A. LCOE reduction for the next generation offshore wind turbines. 2017.
[4] Smart G. Offshore wind cost reduction recent and future trends in the UK and europe. 2016.
[5] Energy Uk. Offshore wind market development and cost reduction background. 2018.
[6] Mehmanparast A, Brennan F, Tavares I. Fatigue crack growth rates for offshore wind monopile weldments in air and seawater: SLIC inter-laboratory test results. Mater Des 2017;114:494–504.
[7] Manwell JF, McGowan JG, Rogers AL. Wind energy explained: theory, design and application. 2009.
[8] Scharff R, Siems M. Monopile foundations for offshore wind turbines - solutions for greater water depths. 2013.
[9] Musial W, Butterfield S, Ram B. Energy from offshore wind. In: Offshore technology conference; 2006. p. 1–11.
[10] Velarde J. Design of monopile foundations to support the DTU 10 MW offshore wind turbine. 2016.
[11] van der Tempel J, Diepeveen NFB, Cerda Salzman DJ, de Vries WE. Design of support structures for offshore wind turbines. WIT Transactions on State of the Art in Science and Engineering 2010;44:1–25.
[12] Arany L, Bhattacharya S, Macdonald J, Hogan SJ. Design of monopiles for offshore wind turbines in 10 steps. Soil Dynam Earthq Eng 2016;92:126–52.
[13] Jacob A, Oliveira J, Mehmanparast A, Hosseinzadeh F, Kelleher J, Berto F. Residual stress measurements in offshore wind monopile weldments using neutron diffraction technique and contour method. Theor Appl Fract Mech 2018;96:418–27.
[14] Igwemezie V, Mehmanparast A, Kolios A. "Current trend in offshore wind energy sector and material requirements for fatigue resistance improvement in large wind turbine support structures–A review. Renew Sustain Energy Rev 2019;101:181–96.
[15] Peeringa J, Bedon G. Fully integrated load analysis included in the structural reliability assessment of a monopile supported offshore wind turbine. Energy Procedia 2017;137:255–60.
[16] Velarde J, Bachynski EE. Design and fatigue analysis of monopile foundations to support the DTU 10 MW offshore wind turbine. Energy Procedia 2017;137:3–13.
[17] Mehmanparast A, Taylor J, Brennan F, Tavares I. Experimental investigation of mechanical and fracture properties of offshore wind monopile weldments: SLIC interlaboratory test results. Fatig Fract Eng Mater Struct 2018:1–17.
[18] ASTM Standard E647 − 13a. Standard test method for measurement of fatigue crack growth rates. Am. Soc. Test. Mater. 2014;03.01.
[19] British Standard Institution. BS ISO 12108:2012, Metallic materials - fatigue testing - fatigue crack growth method. 2012. London.
[20] American Society For Testing and Materials - ASTM D1141. Standard practice for the preparation of substitute ocean water. *ASTM Int.*; 2013.
[21] Paris PC, Erdogan F. A critical analysis of crack propagation laws. *ASME*; 1963. p. 528–33.
[22] Paris PC. A note on the variables affecting the rate crack growth due to cyclic loading. *Boeing Company*; 1957. Doc. No. D-17867, Add. N.
[23] Paris PC. Crack propagation caused by fluctuating loads. ASME 1962;62.
[24] Paris PC, Gomez MP, Anderson WE. A rational analytic theory of fatigue. Trend Eng 1961;13(1):9.
[25] Kumar V, German MD, Shih CF. Engineering approach for elastic-plastic fracture analysis. General Electric Co; 1981 (No. EPRI-NP–1931).
[26] Ramberg W, Osgood WR. Description of stress-strain curves by three parameters. 1943.
[27] Mehmanparast A. The influence of inelastic damage on creep, fatigue and fracture toughness. Imperial College London; 2012.
[28] Igwemezie V, Mehmanparast A, Kolios A. Materials selection for XL wind turbine support structures: a corrosion-fatigue perspective. Mar Struct 2018;61(June 2018):381–97.
[29] The British Standards Institution. BSI Standards Publication Guide to methods for assessing the acceptability of flaws in metallic structures. 2015.
[30] Adedipe O, Brennan F, Mehmanparast A, Kolios A, Tavares I. Corrosion fatigue crack growth mechanisms in offshore monopile steel weldments. Fatig Fract Eng Mater Struct 2017;40(11):1868–81.
[31] Fukuda T, Iwadate T, Shimazaki M. Consideration on the scatter of COD and fatigue crack propagation characteristics of heavy section C-Mn-V forged steel for offshore structure. Offshore Technol. Conf. 1982:109–12.
[32] Havn T, Osvoll H. Corrosion fatigue of steel in seawater. In: NACE international corrosion conference; 2002. p. 1–11.
[33] Lieb K, Horstman R, Power B, Meltzer R, Vieth M, Vosikovsky O. Effects of stress ratio on fatigue crack growth rates in X70 pipeline steel in air and saltwater. J Test Eval 1980;8(2):68–73.
[34] Zhang W, Brook R. The effect of loading sequence on fatigue crack growth of an offshore structural steel. In: International offshore and polar engineering conference; 1993. p. 98–103.
[35] Abramoff MD, Magalhaes PJ, Ram SJ. Image processing with ImageJ. Biophot Int 2004;11(7):36–42.
[36] Ermakova A, Mehmanparast A, Ganguly S, Razavi J, Berto F. Investigation of mechanical and fracture properties of wire and arc additively manufactured low carbon steel components. Theor Appl Fract Mech 2020;109:102685.
[37] Mehmanparast A, Davies CM, Dean DW, Nikbin KM. Plastic pre-compression and creep damage effects on the fracture toughness behaviour of Type 316H stainless steel. Eng Fract Mech 2014;131:26–37.
[38] Mehmanparast A, Davies CM, Dean DW, Nikbin KM. The influence of pre-compression on the creep deformation and failure behaviour of Type 316H stainless steel. Eng Fract Mech 2013;110:52–67.
[39] Mehmanparast A, Davies CM, Dean DW, Nikbin K. Effects of plastic pre-straining level on the creep deformation, crack initiation and growth behaviour of 316H stainless steel. Int J Pres Ves Pip 2016;141:1–10.